An improved transfer-matrix model for optical superlenses

Ciaran P. Moore,[1] Richard J. Blaikie,[1,*] and Matthew D. Arnold[2]

[1]MacDiarmid Institute for Advanced Materials and Nanotechnology, Department of Electrical and Computer Engineering, University of Canterbury, Private Bag 4800, Christchurch, New Zealand.
[2]Institute for Nanoscale Technology, Department of Physics and Advanced Materials, University of Technology Sydney, PO Box 123 Broadway, NSW 2007, Australia.
* richard.blaikie@canterbury.ac.nz

Abstract: The use of transfer-matrix analyses for characterizing planar optical superlensing systems is studied here, and the simple model of the planar superlens as an isolated imaging element is shown to be defective in certain situations. These defects arise due to neglected interactions between the superlens and the spatially varying shadow masks that are normally used as scattering objects for imaging, and which are held in near-field proximity to the superlenses. An extended model is proposed that improves the accuracy of the transfer-matrix analysis, without adding significant complexity, by approximating the reflections from the shadow mask by those from a uniform metal layer. Results obtained using both forms of the transfer matrix model are compared to finite element models and two example superlenses, one with a silver monolayer and the other with three silver sublayers, are characterized. The modified transfer matrix model gives much better agreement in both cases.

OCIS codes: (310.6628) Subwavelength structures, nanostructures; (310.6860) Thin films, optical properties; (260.2110) Electromagnetic optics; (240.6680) Surface plasmons.

References and links

1. J. B. Pendry, "Negative refraction makes a perfect lens," Phys. Rev. Lett. 85(18), 3966–3969 (2000).
2. S. A. Ramakrishna, J. B. Pendry, D. Schurig, D. R. Smith, and S. Schultz, "The asymmetric lossy near-perfect lens," J. Mod. Opt. 49(10), 1747–1762 (2002).
3. S. A. Ramakrishna, et al., "Imaging the near field," J. Mod. Opt. 50, 1419–1430 (2003).
4. D. O. S. Melville, and R. J. Blaikie, "Analysis and optimization of multilayer silver superlenses for near-field optical lithography," Phys. Rev. B 394, 197–202 (2007).
5. D. R. Smith, D. Schurig, M. Rosenbluth, S. Schultz, S. A. Ramakrishna, and J. B. Pendry, "Limitations on subdiffraction imaging with a negative refractive index slab," Appl. Phys. Lett. 82(10), 1506–1508 (2003).
6. C. P. Moore, M. D. Arnold, P. J. Bones, and R. J. Blaikie, "Image fidelity for single-layer and multi-layer silver superlenses," J. Opt. Soc. Am. A 25(4), 911–918 (2008).
7. K. Lee, Y. Jung, G. Kang, H. Park, and K. Kim, "Active phase control of a Ag near-field superlens via the index mismatch approach," Appl. Phys. Lett. 94(10), 101113 (2009).
8. P. Andrew, and W. L. Barnes, "Energy transfer across a metal film mediated by surface plasmon polaritons," Science 306(5698), 1002–1005 (2004).
9. D. O. S. Melville, and R. J. Blaikie, "Super-resolution imaging through a planar silver layer," Opt. Express 13(6), 2127–2134 (2005).
10. N. Fang, H. Lee, C. Sun, and X. Zhang, "Sub-diffraction-limited optical imaging with a silver superlens," Science 308(5721), 534–537 (2005).
11. D. O. S. Melville, and R. J. Blaikie, "Experimental comparison of resolution and pattern fidelity in single- and double-layer planar lens lithography," J. Opt. Soc. Am. B 23(3), 461–467 (2006).
12. O. S. Heavens, Optical properties of thin solid films (Butterworths Scientific Publications, London, 1955), Chap. 4.
13. P. Pereyra, "Resonant tunneling and band mixing in multichannel superlattices," Phys. Rev. Lett. 80(12), 2677–2680 (1998).
14. J. Jia, The finite element method for electromagnetics (Wiley, New York, 1993).
15. P. Pereyra, A. Robledo-Martinez, and M. Morales-Luna, "The effect of complex and negative indices in the transmission of electromagnetic waves through superlattices," Microelectron. J. 39(3-4), 394–397 (2008).
16. COMSOL is a registered trademark of COMSOL A.B., (1997–2009).

17. P. Bienstman, Rigorous and efficient modelling of wavelength scale photonic components, PhD. Thesis (Ghent University, Belgium, 2001), Chap. 4.
18. C. P. Moore, R. J. Blaikie, and M. D. Arnold, "Improved analytical models for single- and multi-layer silver superlenses," Proc. 2009 MRS Spring Meeting 1182, in press (2009).
19. P. B. Johnson, and R. W. Christy, "Optical constants of the noble metals," Phys. Rev. B 6(12), 4370–4379 (1972).
20. J. B. Pendry, and A. MacKinnon, "Calculation of photon dispersion relations," Phys. Rev. Lett. 69(19), 2772–2775 (1992).
21. L. C. Botten, M. S. Craig, R. C. McPhedran, J. L. Adams, and J. R. Andrewartha, "Highly conducting lamellar diffraction gratings," J. Mod. Opt. 28(8), 1087–1102 (1981).
22. M. G. Moharam, E. B. Grann, D. A. Pommet, and T. K. Gaylord, "Formulation for stable and efficient implementation of the rigorous coupled-wave analysis of binary gratings," J. Opt. Soc. Am. A 12(5), 1068–1076 (1995).
23. S. A. Ramakrishna, "Physics of negative refractive index materials," Rep. Prog. Phys. 68(2), 449–521 (2005).
24. A. Z. Ultra-i, ™ 123 data sheet © 2005 Rohm and Haas Electronic Materials. http://www.microresist.de/products/room_haas/pdf/ULTRA-i_123_Serie.pdf, retrieved on 18 July 2009.

1. Introduction

Optical superlenses [1] have been the subject of several significant and important predictions in recent times: minimum resolution well below the operating wavelength [1,2] and improved resolution for multi-layer structures compared to single-layer equivalents [3,4] have been predicted, based to a large degree on the results of analytical studies [5–7]. A limited supply of experimental data [8–11] has confirmed the qualitative aspects of many of these predictions, but little work has been done to verify the quantitative estimates suggested by such analytical reports.

This paper aims to address the quantitative accuracy of analytical superlens models by comparing the results of a popular model [4,6,12,13] consisting of isolated superlenses within a transfer-matrix method (TMM) framework to rigorous, fully-coupled solutions of Maxwell's equations obtained via finite element modeling (FEM) [14]. We find significant quantitative differences between TMM analysis and FEM results, which we attribute to near-field mask-superlens interactions that are not accounted for in the simple system models normally used in TMM studies. We propose a modified transfer-matrix model (M-TMM) that can treat such mask-superlens interactions approximately, and we compare M-TMM- and FEM-generated data sets to quantify the improved accuracy that results.

2. Theory

The behaviour and super-resolving performance of metallo-dielectric near-field superlenses is mediated by surface plasmon resonances (SPs), rather than being a pure negative-refraction phenomenon for a 'perfect' lens [1]: electrons on the surfaces of metallic layers within the superlens are excited into SP standing waves by incoming electromagnetic waves, and it is the interference between these that is detected by an electro-sensitive photoresist at the exit plane of the superlens. Importantly, the low total thickness of the superlens prevents the enhanced, localized electric fields in the SPs from dispersing significantly within the lens; hence contrast is maintained between bright, electrically-excited areas and dark areas where there is very little increase in electric field.

In effect, the increased electric fields represent enhancements to the evanescent waves scattered from the object. These contain the majority of the sub-diffraction limit information about the object but are normally attenuated to negligible levels beyond the near field (~λ/10). Their enhancement and subsequent interaction with the photoresist at the image plane of the superlens leads to the formation of images with detail much finer than the wavelength of incident light.

Superlens' imaging behaviour can be conveniently described by spatial-frequency transfer functions, examples of which are shown in Fig. 1. Such transfer functions have been calculated and reported regularly using analytical TMM techniques [4–6,15], but usually for the isolated superlens, rather than for the near-field-coupled mask-lens-detector system; the transfer functions in Fig. 1 have been calculated using a full-vector simulation model based on Maxwell's equations, which includes the near-field mask-lens interactions (for a 40-nm thick

tungsten mask typical of experiments [9,11]). This model was implemented using the FEM-based COMSOL Multiphysics engine [16], and was independently verified by cavity modeling framework (CAMFR) [17] simulations. Full details for our technique of extracting the transfer function from such FEM and/or CAMFR simulations are reported elsewhere [18].

The transfer function for an 80-nm thick silver superlens (40 nm of silver symmetrically placed between silica dielectric spacers and illuminated at a wavelength of 365 nm) is shown in Fig. 1. The resonant peak at ~9 μm^{-1} in the characteristic curve is representative of the SP-enhanced behavior of the evanescent fields in such systems but, as we show later, the size and position of this feature does not agree well with conventional TMM results. The transfer function for an 80 nm pure-dielectric gap (dashed line) is also shown, to draw attention to the much higher transmission by the superlens of evanescent (sub-wavelength) wave numbers. The full details of the systems used in this example, and the example of a triple-layer lens presented later, are given in Table 1.

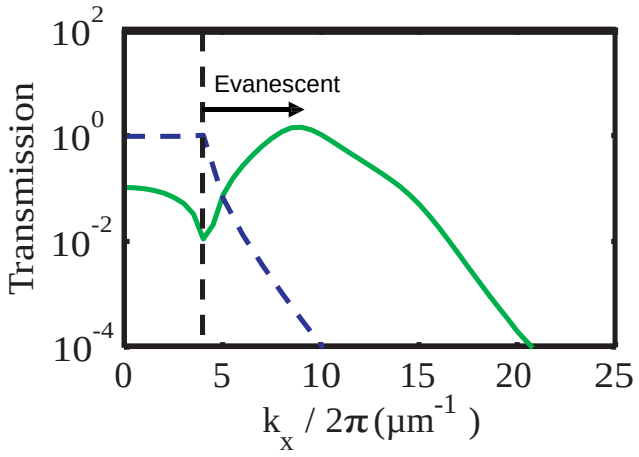

Fig. 1. Spatial-frequency transfer functions for the dielectric gap (dashed) and superlens (solid) described in Table 1. Both curves are generated from full-vector FEM simulations. The spatial frequency modes are evanescent to the right of the vertical line at 4.2 μm^{-1}.

Table 1. Materials and dimensions of systems studied. Illumination wavelength is 365 nm and a 40-nm thick tungsten mask layer ($\varepsilon_{r\,W} = -1.497 + 7.690i$) has been used in all cases.

Lens	Materials	Properties	Dimensions
Dielectric gap	SiO_2	$\varepsilon_{r\,gap} = 2.368$	80 nm
Single-layer Superlens	SiO_2 / Ag / SiO_2	$\varepsilon_{r\,Ag} = -2.7 + 0.23i$ $\varepsilon_{r\,SiO2} = 2.368$	20 / 40 / 20 nm
Multilayer superlens	SiO_2 / Ag / SiO_2 / Ag / SiO_2 / Ag / SiO_2	$\varepsilon_{r\,Ag} = -2.7 + 0.23i$ [19] $\varepsilon_{r\,SiO2} = 2.368$	6.7 / 13.3 / 13.3 / 13.3 / 13.3 / 13.3 / 6.7 nm

3. Analytical model

Calculating transfer functions using full vector electromagnetic simulations requires specialized software and careful setup of the numerical models [18]. Analytical approaches are therefore valuable to simplify the characterization of many-layered superlenses, and a transfer-matrix method (TMM) [4–7] has been widely used by others to date. This technique calculates transmission and reflection coefficients between material interfaces in the superlens stack, and is computationally economical compared to full-vector simulations. The compromise required is that spatial variation along an interface is not normally incorporated and perfectly smooth material boundaries have to be assumed. Rigorous incorporation of mask-lens interactions is technically possible for periodic mask objects [20–22], but the resulting analysis becomes object-specific and requires discretization of the system, so the

attractive simplicity of the 'standard' TMM modeling is lost. We show here how a straightforward modification to the system model used for TMM analysis can be incorporated to provide improved accuracy with little additional complexity.

A TMM-calculated transfer function for the isolated single-layer superlens described in Table 1 is shown in Fig. 2 alongside our FEM-based curve, showing the effects of mask-lens interaction. Three features are of interest in Fig. 2: firstly, the TMM estimate of the zero-frequency (DC) coefficient is larger by a factor of three compared to the FEM estimate; secondly, the peak transmission (SP field enhancement) is predicted by TMM to be 12.04 × compared to the FEM calculation of 1.485 × ; and, thirdly, the wave-number at which this occurs is underestimated by the TMM analysis (7.0 ± 0.2 μm^{-1}, compared with 9.0 ± 0.5 μm^{-1} from FEM).

The effects of these differences can be seen in Fig. 3, where both techniques are used to calculate spatial image profiles for a double slit, sub-wavelength mask [23]. The image profile generated using the TMM-derived transfer function without accounting for mask-lens interaction is clearly in error, with the peak intensities in the image being a factor of three higher than those predicted from the full-field FEM simulations. So, whilst the TMM analysis using a simple isolated-superlens model can be used to determine the qualitative features in superlens imaging it will typically over-estimate image intensity.

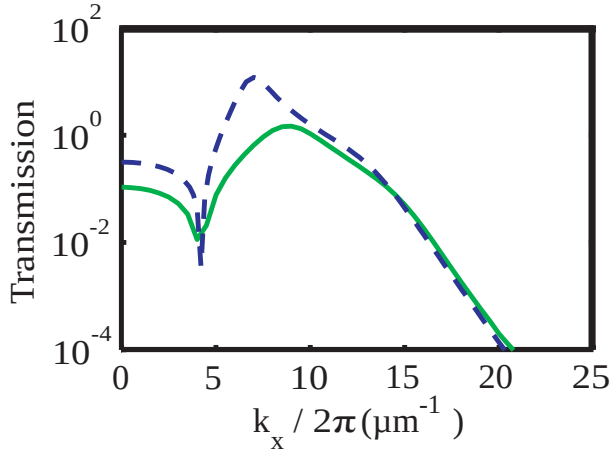

Fig. 2. TMM (dashed) and FEM (solid) generated transfer functions for the superlens described in Table 1.

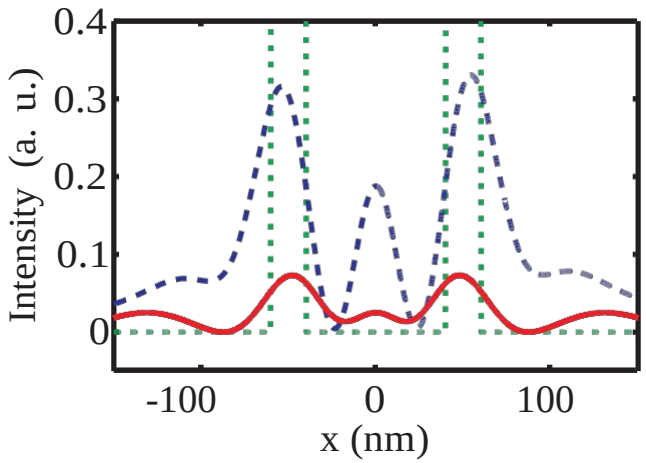

Fig. 3. Output profiles predicted by TMM (dashed) and FEM (solid) for a sub-wavelength mask (dotted) with 20-nm wide apertures on a 100-nm centre-to-centre spacing.

4. Modified transfer-matrix model

Although TMM, which is an exact analytical technique, rigorously models electromagnetic behaviour within a superlens stack, the simple isolated-system model that is normally used neglects the interactions that occur between a mask and the outer-most interface of the lens, which Fig. 2 and 3 showed to be of considerable importance. The reason for this omission is that the spatially-variant features of the mask are orthogonal to the one-dimensional plane that the T-matrix simulation occupies, and thus cannot be represented in the simulation. Hence, a modification to the model is necessary to account for mask features and their resulting effects on lens performance.

One such modification, which we report here, relies on the assumption that, for super-resolution imaging, any features in the mask are likely to be very small compared to the wavelength. This means that reflection from a dark mask with narrow apertures can be approximated by a single, solid slab, constructed of identical material to the mask. Similarly, if the mask contains only small dark features, then it can be approximated by its host medium, and mask-lens interactions can be ignored. Since the analysis for the mostly-light case reduces trivially to that shown in Section 3, consideration is given here to the mostly-dark case. Our essential argument is that reflections from masks with sub-wavelength spacings cause minimal scattering outside zeroth-order, and hence the amplitude and phase of the reflection from mostly-dark masks is typically independent of the apertures. In this paper, we test the accuracy of this assumption for mostly-dark masks, by comparing representative results from analyses using our modified transfer-matrix model (M-TMM) with full-field simulation results.

Our M-TMM technique involves a simple extension of TMM, with the inclusion of first-order mask-superlens reflections. Using TMM (or any other analytical method), a spatial-frequency-dependent reflection function, r_M, can be calculated for the slab-equivalent of the mask; an example of such a reflection function for a 40-nm thick tungsten slab is shown in Fig. 4. Once calculated, r_M is used in combination with the TMM-derived reflection function of the isolated superlens stack, r_L, to calculate the effect that the mask-lens interactions have on the overall transfer function of the super-resolving system.

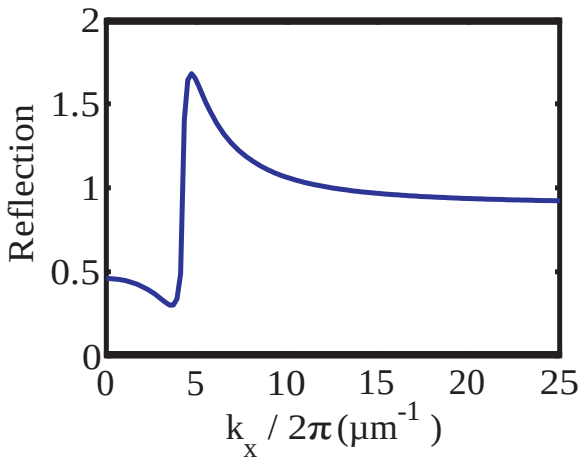

Fig. 4. Spatial-frequency-dependent reflection function for a 40-nm thick tungsten slab.

Figure 5 illustrates the M-TMM calculation. Without considering the mask, an incident signal, ip, is transmitted through the isolated superlens stack according to the TMM-generated transfer function, t, to give an output, op = ip.t. A proportion of ip is also reflected by the lens, giving ip.r_L. When the mask is included in the calculations, ip.r_L is re-reflected according to r_M, and appears at the object plane as ip.r_L.r_M, with r_M including the round-trip phase of exp(−2ikd) between the lens and the mask. The field on the other side of the superlens stack then becomes op = ip.t + ip.r_L.r_M. Just as before, a fraction of this is reflected off the lens and re-reflected off the mask, creating an additional term at the image plane. This series continues ad infinitum, with its sum given by [12,15]

$$op = \frac{ip \cdot t}{1 - r_L \cdot r_M}. \tag{1}$$

This allows us to determine a modified transfer function, t', which includes the infinite sum of reflections between the mask and lens, that can be calculated as

$$t' = \frac{op}{ip} = \frac{t}{1 - r_L \cdot r_M}. \tag{2}$$

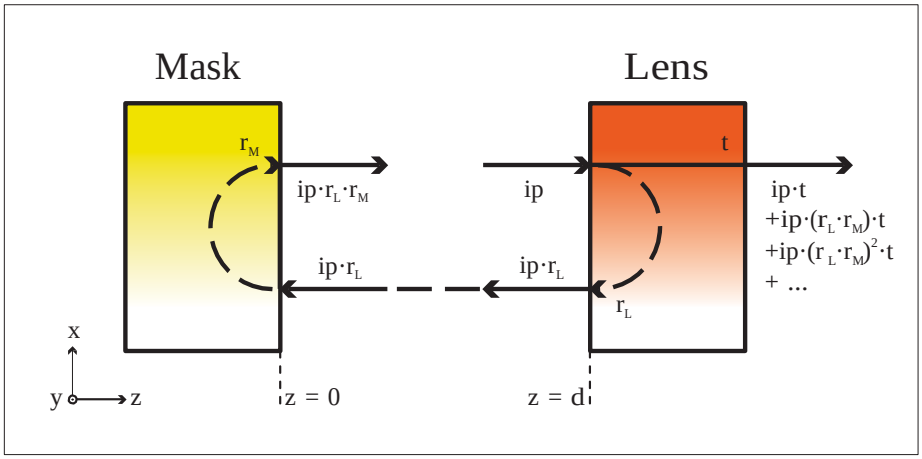

Fig. 5. Recursive mask-lens interactions.

The different transfer functions produced by TMM, M-TMM and the FEM simulation are shown in Fig. 6 for the superlens whose parameters are presented in Table 1. The M-TMM transfer function is clearly a better estimate of system performance than that obtained from TMM with an isolated-lens model, so the simple first-order assumptions we have made have good validity. Agreement is not perfect, and we quantify differences here. Firstly, unlike the simple transfer-matrix model, M-TMM predicts a peak in transmission at the same wave number ($8.8 \pm 0.2\ \mu m^{-1}$) as the FEM simulation ($9.0 \pm 0.5\ \mu m^{-1}$). Predicted peak transmission from M-TMM is not in very good agreement with the FEM result (0.6838 × compared to 1.485 ×); however it is still a much better estimate than obtained using the simple system model (12.04 ×). The zero-frequency (DC) transfer coefficient from M-TMM is higher than the FEM result (0.1727 × compared to 0.1084 ×), but is better than the figure of 0.3172 × for the simple system model.

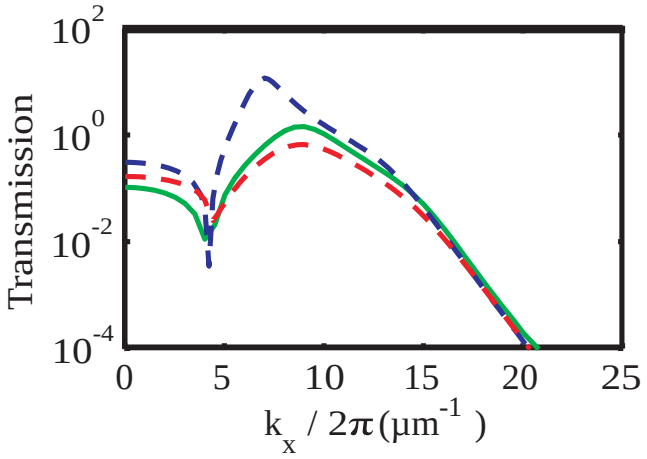

Fig. 6. M-TMM (dotted), TMM (dashed) and FEM (solid) transfer functions for the superlens described in Table 1.

A comparison of image profiles calculated by FEM and M-TMM is shown in Fig. 7 for the same double-slit object used for Fig. 3. In this case the quantitative agreement between the results is very good, again highlighting the fact that our simple, first-order M-TMM accounts for the most significant aspects of mask-lens interactions for imaging sub-wavelength features transmitted through an otherwise-opaque planar screen.

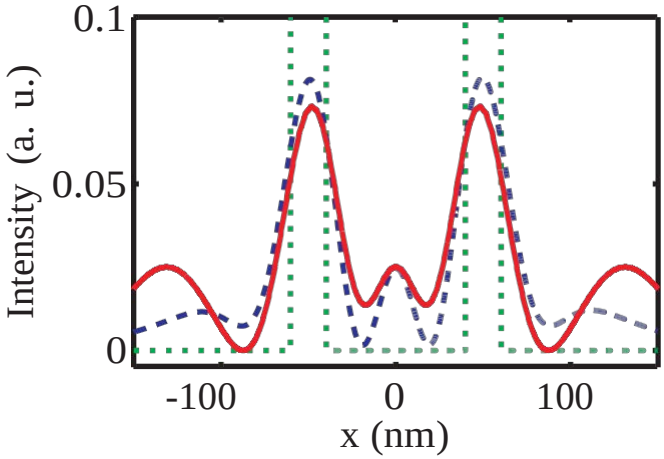

Fig. 7. Output profiles predicted by M-TMM (dashed) and FEM (solid) for a sub-wavelength double- slit mask (dotted).

5. Effects of the detector layer

Given that the superlens performance is influenced significantly by mask-lens interactions it is also natural to consider the effects of near-field interactions with the imaging layer beneath the superlens. We have so far considered the medium beneath the superlens to be lossless silica (or equivalent dielectric), but in practice the imaging layer must have some loss, and may also be mismatched from its surroundings. We will not consider the case of severe mismatch here in detail, as photoresists generally have refractive indices n ~1.7, close to that of silica. But we note that severe mismatch might be expected if imaging was to take place using a scanning near-field optical microscope (SNOM), however we do not consider the variations of SNOM image collection here and how they might be accounted for by further modifications to the TMM models.

What we have studied in detail are the effects of using photolithographic imaging layers, as have been used in optical superlensing experiments [9,10], and we find that these do not affect the quantitative imaging results significantly. Figure 8 shows line traces of the intensity at the imaging plane for the single-layer superlens and the two-slit mask object, with three different imaging layers considered: a lossless medium perfectly index-matched to SiO_2, ε = 2.368 (solid); AZ ultra-i123 photoresist [24] in its unexposed state, $\varepsilon = 2.729 + 0.024i$ (dashed); and the same resist in its fully-bleached state, $\varepsilon = 2.729 + 0.001i$ (dotted). There is a relatively modest (~20%) reduction in the peak intensities for the cases where an absorbing photoresist is modeled, which is due to the combined effects of mismatch with the silica layer and absorption in the resist. However, most significantly, we find no discernable difference in the results for the resist in its bleached or unbleached states, which is not surprising given the small imaginary component in its permittivity, even when it is in its most absorbing state.

We have also studied the case where a non-uniform lateral absorbance profile is present in the resist layer, to represent the situation near the end of the image capture process where the image has been recorded in this layer and some diffraction from this non-uniform absorbance profile might be expected. We find that this does not have a discernable effect on the modeled intensity profile either, which we also attribute to the small imaginary component of the resist's permittivity (any diffraction will be very weak). Hence the effects of the detector layer for photolithographic near-field imaging are not significant, apart from a relatively minor intensity drop due to simple dielectric mismatch and loss; this is straightforward to account for in any TMM model by incorporating an additional dielectric/photoresist interface if this level of accuracy is required.

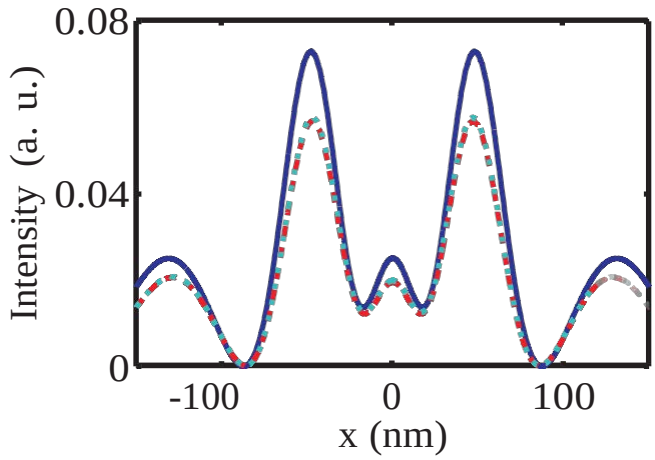

Fig. 8. FEM modeling results for different detector-layer media: lossless SiO_2, ε = 2.368 (solid); AZ ultra-i123 photoresist [24] in its unexposed state, $\varepsilon = 2.729 + 0.024i$ (dashed); and the same resist in its fully-bleached state, $\varepsilon = 2.729 + 0.001i$ (dotted).

6. Multilayer superlens performance example

Modified TMM analysis has also been applied to a triple-layer superlens with the same total thickness as the single-layer example, whose parameters are also described in Table 1. Accurate characterization of such a lens is of special interest, given the attention that multi-layered lenses have received in the literature [3,4]. As seen in Fig. 9, the characteristic differences observed between transfer functions calculated using FEM and a simple TMM model for a single-layer isolated superlens are also present for the multi-layer equivalents: zero-frequency performance varies greatly between techniques and discrepancies remain in the estimates of both the peak transmission and peak wave number. Once again, M-TMM is closer to the FEM-generated results, particularly for the position of the SP peak. The spatial profiles shown in Fig. 10 confirm this conclusion, as do the high correlation coefficients [6] between FEM- and M-TMM-generated transfer functions, shown in Table 2.

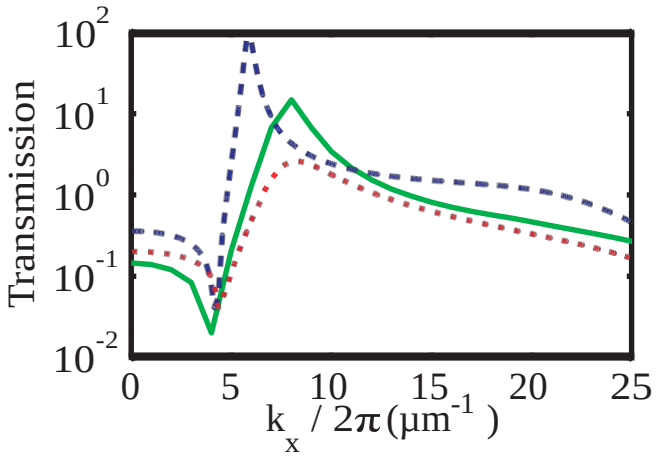

Fig. 9. Modified TMM (dotted), TMM (dashed) and FEM (solid) transfer functions for the multilayer superlens described in Table 1.

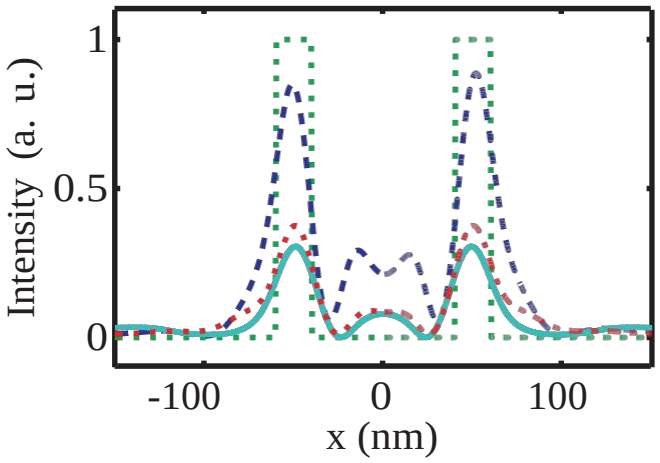

Fig. 10. Output profiles predicted by TMM (dashed), Modified TMM (dot-dashed) and FEM (solid) for a sub-wavelength mask (dotted).

Table 2. Superlens characterization metrics

Parameter	Single-Ag layer superlens			Multi-Ag layer superlens		
	Simple TMM	Modified TMM	FEM	Simple TMM	Modified TMM	FEM
DC transmission coeff.	0.3172	0.1727	0.1084	0.3671	0.2060	0.1465
Peak transmission coeff.	12.04	0.6838	1.485	87.41	2.612	14.88
Peak wave number (μm^{-1})	7.0 ± 0.1	8.8 ± 0.1	9.0 ± 0.2	5.9 ± 0.1	8.3 ± 0.1	8.0 ± 0.5
Correlation to FEM	0.2380	0.9894	1.0000	−0.0411	0.8356	1.0000

7. Conclusion

The numerical results presented in Table 2, together with the transfer functions shown in Figs. 6 and 9 and the spatial profiles presented in Figs. 7 and 10 show that results found using a simple, isolated-superlens model in TMM analyses are not inherently good approximations of full-wave vector analyses or of real-world performance. The artifacts in these results are addressed to a large extent by the proposed modified transfer-matrix model, which provides better estimates of peak wave number and overall transfer function shape. This is the case regardless of the type of superlens (single- or multi-layered) under consideration.

Future work will focus on extension of the M-TMM technique to obtain better estimates of the mask reflectivity function; it is the small differences in this reflectivity to which we attribute residual inaccuracies in the method. In addition, it will be interesting to study the case of masks with dense periodic or quasi-periodic objects of arbitrary duty cycles, as it should be possible to estimate these masks' reflectivity functions in the sub-wavelength limit using effective-medium theory. Ultimately, comparison with experimental results will be the best way of determining how much additional sophistication is required from a modeling or simulation tool.

Acknowledgements

This work was supported by the MacDiarmid Institute for Advanced Materials and Nanotechnology and the Marsden Fund administered by the Royal Society of New Zealand. One of us (CPM) also acknowledges financial support from the Department of Electrical and Computer Engineering, University of Canterbury.